Rational synthesis of ternary PtIrNi nanocrystals with enhanced poisoning tolerance for electrochemical ethanol oxidation

Yahia H. Ahmad[a], Assem T. Mohamed[a], Khaled M. Youssef[b], Subhajit Kundu[c], K. Andre Mkhoyan[c], Siham Y. Al-Qaradawi[a],*

[a] Department of Chemistry and Earth Sciences, College of Arts and Sciences, Qatar University, Doha 2713, Qatar
[b] Materials Science and Technology Master Program, Qatar University, Doha 2713, Qatar
[c] Department of Chemical Engineering and Materials Science, University of Minnesota, Minneapolis, MN 55455-0132, USA

ABSTRACT

The development of highly efficient and durable anode materials for ethanol electro-oxidation remains a challenge. Herein, we report the synthesis of $Pt_{1-x-y}Ir_xNi_y$ nanocrystals via one-step procedure by ultrasonic-assisted co-reduction of the metal precursors using ascorbic acid as a mild reducing agent and pluronic F127 as a structure directing agent. The catalytic performance of this ternary catalyst towards electrochemical oxidation of ethanol was examined and compared to its mono and binary Pt counterparts (Pt, $Pt_{1-x}Ir_x$, and $Pt_{1-y}Ni_y$) that are synthesized by the same method. TEM analysis showed a porous nanodendritic structure for the synthesized ternary electrocatalyst with an average size of $20 \pm 1\,nm$. The electrochemical measurements revealed an electrochemically active surface area, ECSA, of $73\,m^2\,g^{-1}$. The as-synthesized ternary electrocatalyst showed an improved catalytic activity towards ethanol oxidation in 1 M KOH with a measured mass activity of $3.8\,A\,mg^{-1}$ which is 1.7, 2.0, and 3.2 times higher than that of $Pt_{1-x}Ir_x$, $Pt_{1-y}Ni_y$, and Pt, respectively. Additionally, the $Pt_{1-x-y}Ir_xNi_y$ nanocrystals expressed high poisoning tolerance ($j_f/j_b = 4.5$) and high durability compared to its mono and binary counterparts.

1. Introduction

Direct ethanol fuel cells (DEFCs) have received great attention in the last decades due to their high energy density, ease of storage, low toxicity, and facile production of fuel from biomass [1–3]. Pt is used extensively as catalyst anode in DEFCs owing to its great catalytic performance towards ethanol electro-oxidation. However, the low tolerance of Pt to poisoning by intermediate species such as CO and CH_x and the absence of long-term stability prohibit its wide commercialization [4,5]. Various approaches have been devoted to improve the stability and catalytic activity of Pt towards ethanol oxidation. Among them alloying of Pt with other metals such as Pd, Ni, Cu, Au, and Ru is particularly promising [6–9]. This is attributed to the modulation of the d-band center, which can tune the electronic structure and consequently enhance the catalytic performance of Pt [10]. It is also believed that alloying of Pt with other metals can tune the adsorbate bonding, support different pathway for the electrochemical reaction, and create multiple active sites. This will allow to overcome the energy barriers for efficient ethanol oxidation i.e. C—C bond cleavage, removing of C1 intermediate species and high selectivity for CO_2 formation [11].

Among different alloying elements, iridium (Ir) has received more attention ascribed to its relatively high oxidation potential of 1.26 V (Ir^{3+}/Ir vs. SCE) and high stability in acidic media [12]. Iridium also displays a high affinity for oxygenated species like O, OH at low overpotentials, which facilitates the oxidation of CO and other intermediates produced at the Pt active sites during the oxidation reaction. Hence it enhances the poisoning tolerance of Pt [13,14]. In addition to Ir, Ni enhances the alcohol oxidation reaction and the nickel oxide formed at low negative potential can also reduce the CO poisoning of Pt by providing of oxygen and easing its oxidation to CO_2 [15]. Integration of Ir and Ni into Pt lattice to form ternary $Pt_{1-x-y}Ir_xNi_y$ alloy is expected to enhance the catalytic performance and poisoning tolerance of Pt towards ethanol oxidation. Enhancements of electrocatalytic activity in other Pt-based ternary alloys in comparison with pure Pt and its binary counterparts have been reported [16–19].

Composition of ternary alloys is not the only factor determining its catalytic activity and stability. The morphology of the nanocrystals can also have a substantial effect on the catalytic performance. Among multifarious morphologies of Pt-based nanocrystals, porous nanodendrites have recently received great interest due to their large surface

---

Table 1
The elemental composition of different catalysts.

Sample	Pt molar percentage %	Ir molar percentage %	Ni molar percentage %
$Pt_{1-x-y}Ir_xNi_y$	84.7	13.9	1.4
$Pt_{1-x}Ir_x$	82.6	17.4	–
$Pt_{1-y}Ni_y$	98.3	–	1.7
Pt	100	–	–

areas and high density of under-coordinated surface atoms [20,21].

Herein we reported the synthesis of porous ternary $Pt_{1-x-y}Ir_xNi_y$ nanodendrites using a facile one-step route. This was achieved by ultrasonic irradiation-assisted co-reduction of the metal precursors using ascorbic acid as a reducing agent and pluronic as a structure directing agent. The fabricated Pt-based ternary electrocatalyst was characterized by transmission electron microscopy (TEM) and X-ray photoelectron spectroscopy (XPS). The catalytic performance towards electrochemical ethanol oxidation in alkaline media was also investigated.
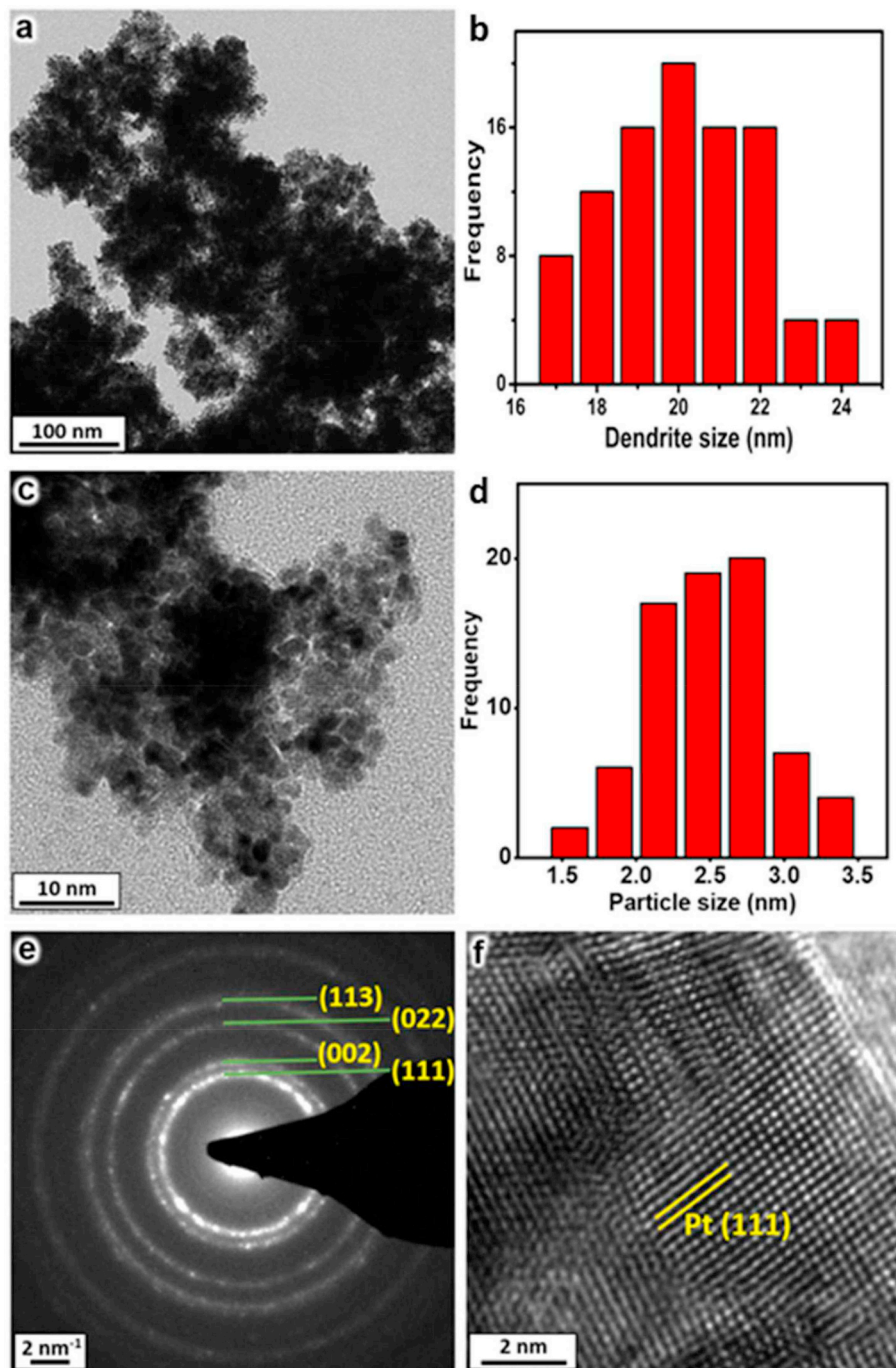

Fig. 1. (a) Low-magnification BF-TEM image of a typical $Pt_{1-x-y}Ir_xNi_y$ nanoparticle dendrites. (b) A histogram of dendrite size yields 20 ± 1 nm. (c) Higher magnification BF-TEM image of a $Pt_{1-x-y}Ir_xNi_y$ single dendrites. (b) A histogram of dendrite forming nanoparticle size yields 2.4 ± 0.4 nm. (e) SAED pattern from the aggregates shows that the particles are crystalline and randomly oriented with respect to each other. (f) A high resolution-TEM image of $Pt_{1-x-y}Ir_xNi_y$ nanocrystals with resolved (111) planes.
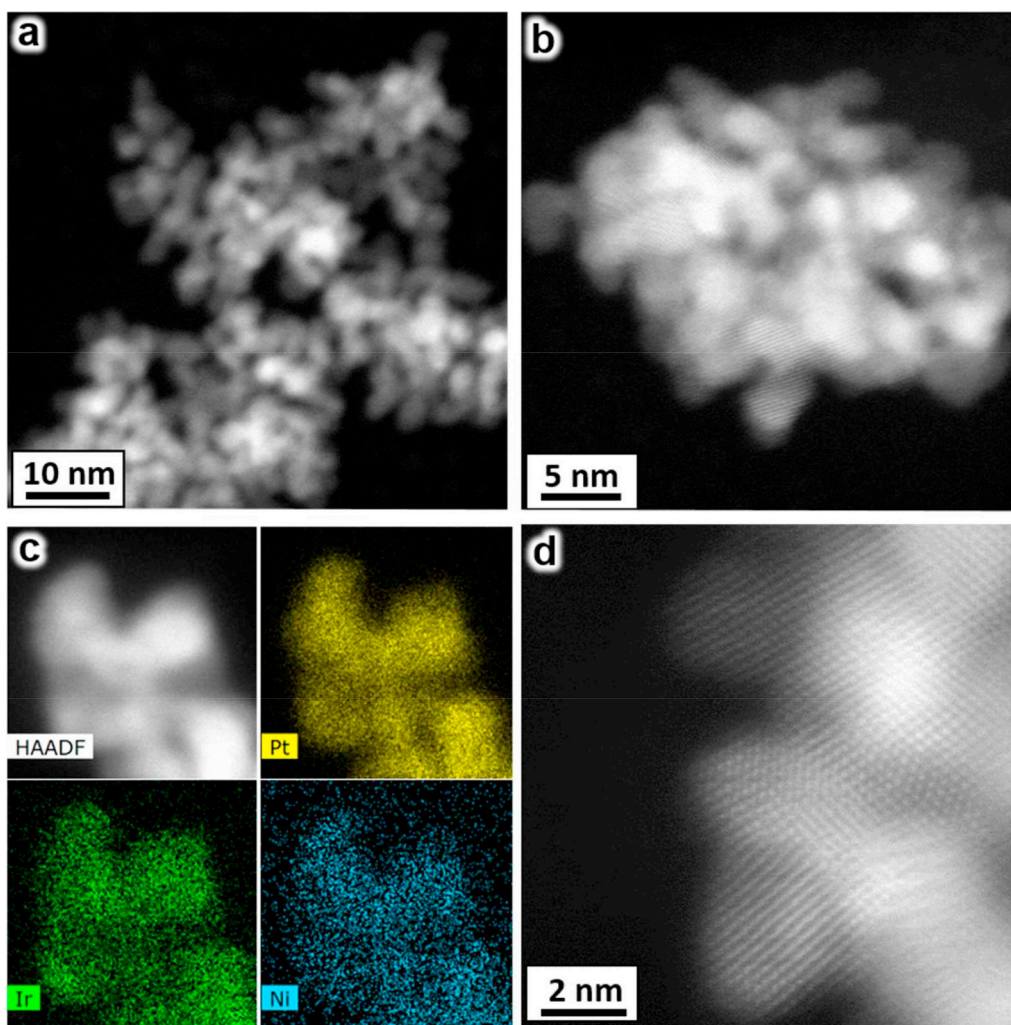
Fig. 2. (a, b) ADF-STEM images of $Pt_{1-x-y}Ir_xNi_y$ nanoparticle aggregate showing uniform contrast across individual nanoparticles. (c) ADF-STEM image and corresponding EDS elemental maps of Pt-L, Ir-L and Ni-K displaying homogenous distribution of the constituent elements. (d) Aromic-resolution ADF-STEM images of $Pt_{1-x-y}Ir_xNi_y$ nanoparticles.

2. Experimental

2.1. Materials and methodology

Porous $Pt_{1-x-y}Ir_xNi_y$ nanocrystals were synthesized via (i) continuous ultrasonic irradiation for 2 h in aqueous solution containing K_2PtCl_4 (2 mL, 20 mM), $IrCl_3$ (1 mL, 20 mM), $NiCl_2$ (1 mL, 20 mM), and 40 mg pluronic F127 and (ii) reduction by addition of ascorbic acid (1 mL, 0.3 M) to the reaction mixture at room temperature. The produced nanocrystals were collected via centrifugation and washed with water and ethanol to remove the impurities. $Pt_{1-x}Ir_x$, $Pt_{1-y}Ni_y$, and Pt nanocrystals were also synthesized with the same procedure using the corresponding metal ions solutions for comparison purposes with the $Pt_{1-x-y}Ir_xNi_y$ nanocrystals.

2.2. Characterization

The compositions of nanocrystals were investigated by inductively coupled plasma atomic emission spectroscopy, ICP-OES (all details are given in the supplementary part). The chemical composition and the valence states of elements were examined via an XPS spectrophotometer (Kratos Axis Ultra XPS) equipped with a monochromatic Al-Kα radiation source (1486.6 eV) under UHV environment (ca.

5×10^{-9} Torr). All binding energies were calibrated to the C 1s peak at 284.8 eV. The particle size, morphology, and composition of electrocatalysts were examined using an aberration-corrected (probe-corrected) FEI Titan™ 60–300 scanning and TEM, which is equipped with high-efficiency Super-X system for energy dispersive X-ray spectroscopy (EDS) [22,23].

Electrochemical measurements were carried out in a three-electrode cell using a Gamry electrochemical station (reference 3000, Gamry Co., USA). A platinum wire, Hg/Hg_2Cl_2 (saturated KCl), and a glassy carbon electrode (GCE, 5 mm diameter) were used as a counter, reference, and working electrodes, respectively. The working electrode was prepared by applying a thin layer of the electrocatalyst on the surface of GCE. The electrocatalyst ink solution was prepared by dispersing 1 mg of the catalyst in 900 μl of water and 100 μl of Nafion solution (0.5% in ethanol). The suspension was sonicated for 30 min, then 6 μl of the well-dispersed catalyst was applied on the GCE surface and dried prior to electrochemical tests. All cyclic voltammetry measurements were performed in N_2-purged solutions at a scan rate of 50 mV s^{-1}. The active electrochemical surface areas (ECSAs) were calculated by the following equation: ECSA = Q_H / m × 210, where Q_H is the charge for hydrogen adsorption, m is the loading amount of Pt on the surface, and 210 μC cm^{-2} is the charge required for monolayer adsorption of hydrogen onto the Pt surface.
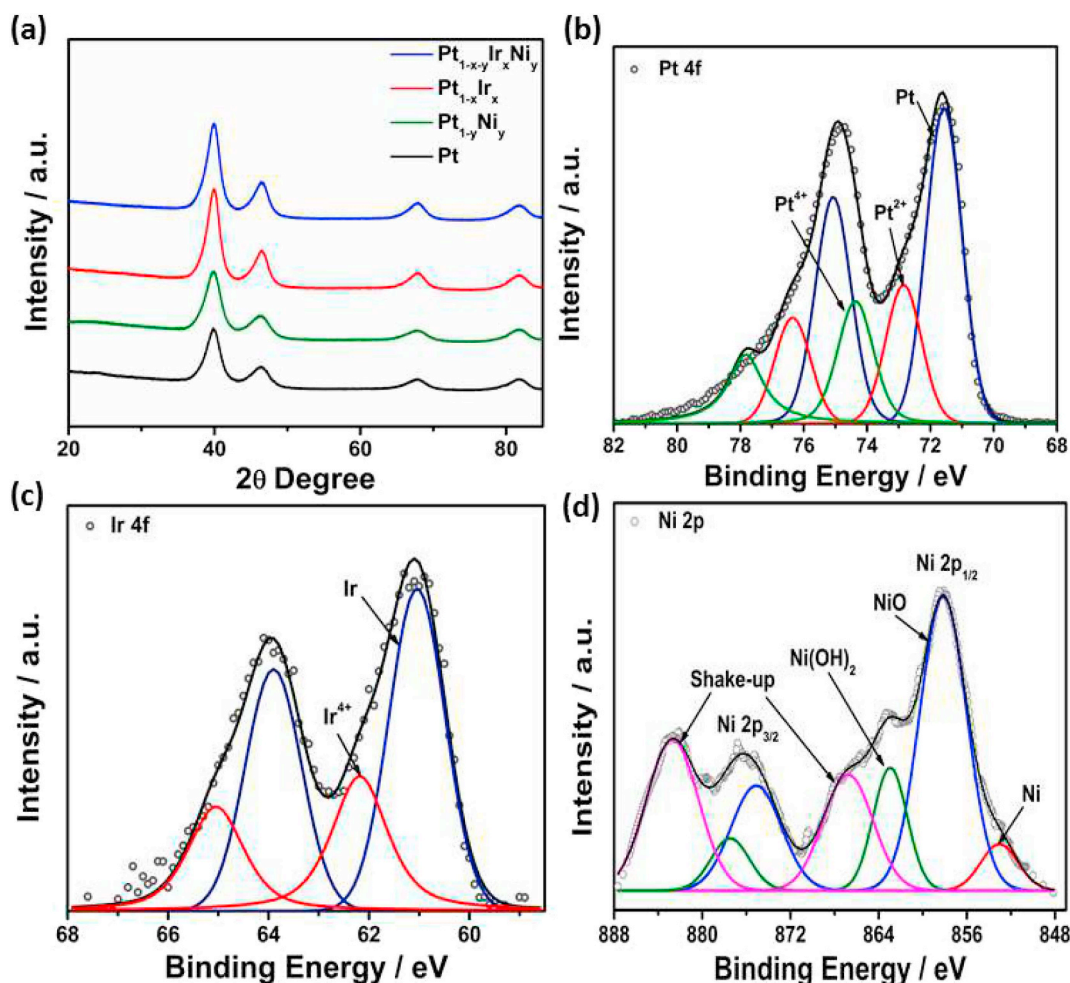
Fig. 3. XRD patterns of as-synthesized materials (a) and high resolution XPS spectra of (b) Pt 4f, (c) Ir 4f, and (d) Ni 2p.

3. Results and discussion

The $Pt_{1-x-y}Ir_xNi_y$ nanocrystals were synthesized by ultrasound-assisted reduction of metal precursors in the presence of pluronic F127 as a structure directing agent. The composition of the as-synthesized nanocrystals was analyzed by (ICP-OES) and results are given in Table 1. Fig. 1a shows a low-magnification bright-field (BF) TEM image of these synthesized ternary $Pt_{1-x-y}Ir_xNi_y$ particles. The image shows porous aggregates of nanocrystals with multiple branches forming dendritic structures. The dendritic particle size distribution obtained from the TEM analysis indicates an average size of 20 ± 1 nm (Fig. 1b). Higher magnification BF-TEM images show that these dendritic particles are composed of smaller nanoparticles with average size of 2.4 ± 0.4 nm (Fig. 1c, d). Similar morphologies and sizes were observed for the $Pt_{1-x}Ir_x$, $Pt_{1-y}Ni_y$, and Pt nanocrystals (see Supplementary Fig. S1). Selected area electron diffraction (SAED) pattern obtained from dendritic aggregates shows rings of identifiable spots indicating that they are collections of multiple nanocrystals of random orientation (Fig. 1e). Analysis of the SAED pattern reveals that the rings correspond to (111), (002), (022), and (113) atomic planes of the face-centered cubic (fcc) crystal structure of Pt. This observation of a single fcc phase indicates an integration of the of Ir and Ni atoms into the Pt fcc structure. Fig. 1f shows the high-resolution TEM image of the synthesized $Pt_{1-x-y}Ir_xNi_y$ nanocrystals with a lattice fringes distance of 0.24 ± 0.01 nm, which is very close to the distance between (111) planes of the Pt crystal (d_{111} = 0.23 nm) [24].

To gain insights into the distribution of the elements in the ternary nanocrystals, a combination of annular dark-field (ADF) STEM imaging with EDS mapping was performed. Fig. 2a and b shows low magnification ADF-STEM images of typical aggregates of these ternary nanocrystals. No abrupt difference in contrast is observed in individual nanoparticles suggesting proper alloying. Fig. 2c shows the ADF-STEM image and the corresponding EDS elemental maps of the nanocrystals. A uniform distribution of Pt, Ir, and Ni throughout the nanodendrites is observed confirming the homogeneity of the structure. Quantification of the intensities of Pt, Ir, and Ni in the EDS spectrum revealed Pt:Ir:Ni molar ratio of 85.0:14.0:1.0, which is in a good agreement with the results of the ICP-OES. Additional ADF-STEM imaging at higher magnification (Fig. 2d) shows resolved atomic columns with no evidence of element segregations.

Wide angle XRD patterns of as-synthesized materials are given in Fig. 3a. All nanoalloys revealed four diffractions peaks around 2θ values of 39.9, 46.4, 67.8, and 81.7° assigned to (111), (200), (220), and (311) reflections of fcc structure of Pt. No diffraction peaks for the monometallic Ir and Ni are detected confirming the formation of only ternary alloy structure.

XPS analysis was performed to elucidate the composition and electronic structure of the ternary $Pt_{1-x-y}Ir_xNi_y$ electrocatalyst. The survey spectrum confirms the presence of Pt, Ir, and Ni in the ternary electrocatalyst (see Supplementary Fig. S2). The Pt 4f spectra revealed two dominant peaks at 71.5 and 74.8 eV assigned to $4f_{7/2}$ and $4f_{5/2}$, respectively. Deconvolution of Pt 4f peaks showed three couples of peaks, two peaks at 71.6 and 75.1 eV assigned to metallic Pt, the other couple at 72.9 and 76.4 eV assigned to Pt^{2+} species, and the third pair at 74.4 and 77.8 eV assigned for Pt^{4+} species (Fig. 3b). Based on the area of the peaks, the predominant species is metallic Pt, which is
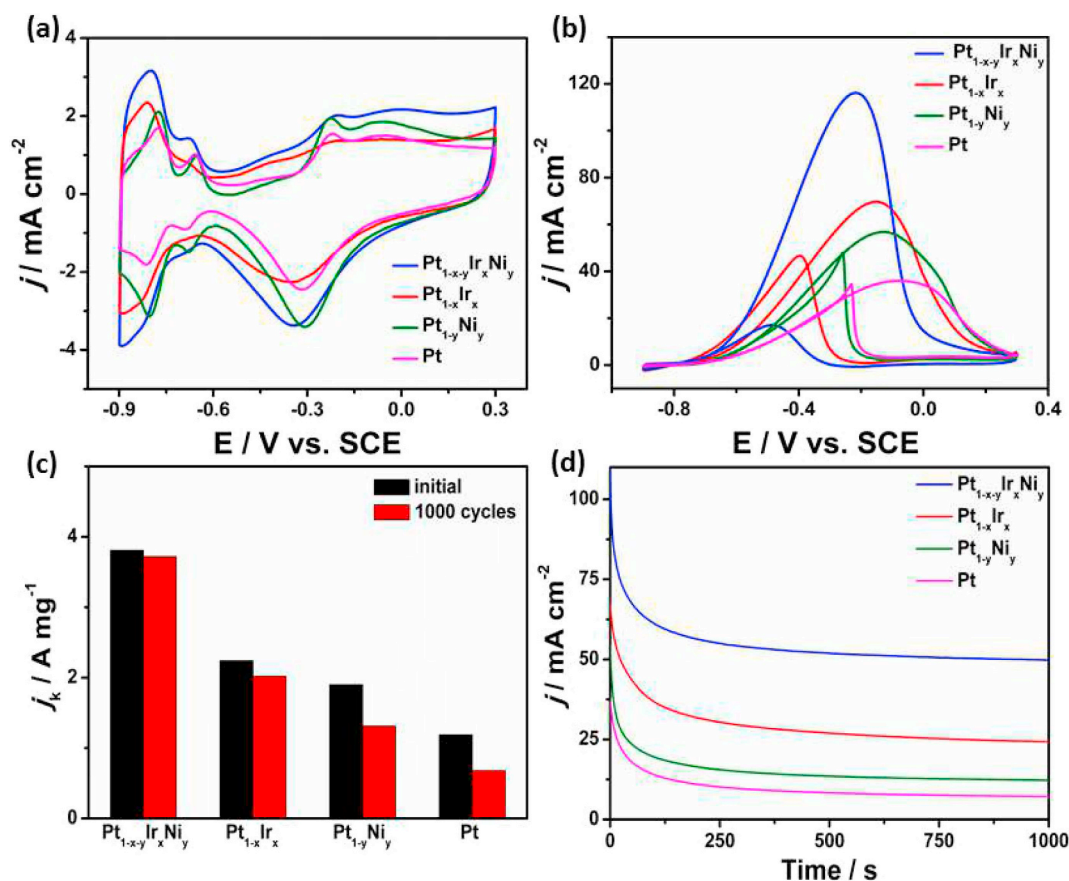
Fig. 4. (a) CV responses of different electrocatalysts in N_2-saturated 1 M KOH, (b) CV responses of different electrocatalysts in 1 M KOH containing 1 M ethanol, (c) mass activities of different electrodes measured initially and after 1000 durability cycles, and (d) chronoamperometric responses of different electrocatalysts at -0.2 V vs. SCE.

Table 2
Summary of electrochemical measurements of different electrocatalysts.

Electrode	ECSA ($m^2 g^{-1}$)	j_f ($mA\,cm^{-2}$)	j_f/j_b	E_{peak} (V vs. SCE)	Mass activity ($A\,mg^{-1}$)	Specific activity ($mA\,cm^{-2}$)
$Pt_{1-x-y}Ir_xNi_y$	72.9	116.7	4.5	-0.22	3.8	5.2
$Pt_{1-x}Ir_x$	51.3	68.6	2.3	-0.16	2.2	4.4
$Pt_{1-y}Ni_y$	43.6	58.3	1.1	-0.13	1.9	4.4
Pt	34.1	36.5	1.2	-0.08	1.2	4.5

expected as shown in previous reports [25]. Deconvolution of high resolution Ir 4f spectra (Fig. 3c) revealed two sets of double peaks. One at binding energies 61.0 and 63.9 eV assigned to metallic Ir, the other pair of peaks at 62.0 and 65.1 eV were assigned to IrO_2 [12]. It is noticeable that metallic Ir is also the prevalent Ir species. High resolution spectrum of Ni 2p is presented in Fig. 3d. The spectrum revealed three peaks in the region of Ni $2p_{3/2}$ at 853.1, 858.1, and 863.0 eV assigned to metallic Ni, NiO, and Ni(OH)$_2$, respectively. The relatively high ratio of oxidized Ni species compared to metallic Ni is due to the oxophilic nature of Ni surface atoms, which have a great tendency to react with atmospheric oxygen and water to form NiO as well as Ni(OH)$_2$ [26].

Fig. 4a depicts the cyclic voltammograms, CV curves of different Pt-based electrocatalysts in N_2-purged 1 M KOH solution at 25 °C. The high values of adsorption/desorption peak currents of hydrogen on $Pt_{1-x-y}Ir_xNi_y$ in comparison to other counterparts provide a clear evidence for its greatest electrochemical active surface area. The values of ECSA for different electrocatalysts were calculated from the CV responses in 1.0 M KOH de-aerated by N_2 and they were found to be 73, 51, 44, and 34 $m^2 g^{-1}$ for $Pt_{1-x-y}Ir_xNi_y$, $Pt_{1-x}Ir_x$, $Pt_{1-y}Ni_y$, and Pt, respectively. Although there is no significant difference between

particle sizes and morphologies for $Pt_{1-x-y}Ir_xNi_y$, $Pt_{1-x}Ir_x$, $Pt_{1-y}Ni_y$, and Pt, the observed differences in the ECSA values may be attributed to the degree of clustering. The high value expressed by ternary nanocrystals can provide more accessible active sites for the reaction and consequently enhance its catalytic activity.

The electrocatalytic activity of the as-synthesized ternary alloy was examined towards ethanol electro-oxidation in an alkaline medium compared to binary and Pt analogues. The catalytic activity was conducted by CV measurements of different Pt-based catalysts in aqueous 1.0 M KOH containing 1.0 M ethanol at a sweep rate of 50 mV s^{-1} in the potential range from -0.9 V to $+0.3$ V vs. SCE (Fig. 4b). All cyclic voltammograms exhibited two well defined peaks, one in the forward scan related to anodic ethanol oxidation reaction and the other is related to the removal of the adsorbed intermediates formed as a result of incomplete oxidation process [27].

The peak current density of $Pt_{1-x-y}Ir_xNi_y$ nanocrystals is 117 mA cm^{-2}, which is almost 1.7, 2, and 3.2 times greater than its value in the case of $Pt_{1-x}Ir_x$, $Pt_{1-y}Ni_y$, and Pt, respectively. The onset potential of ethanol electro-oxidation in case of $Pt_{1-x-y}Ir_xNi_y$ is -0.22 V vs. SCE whereas its value is -0.16, -0.13, and -0.08 V
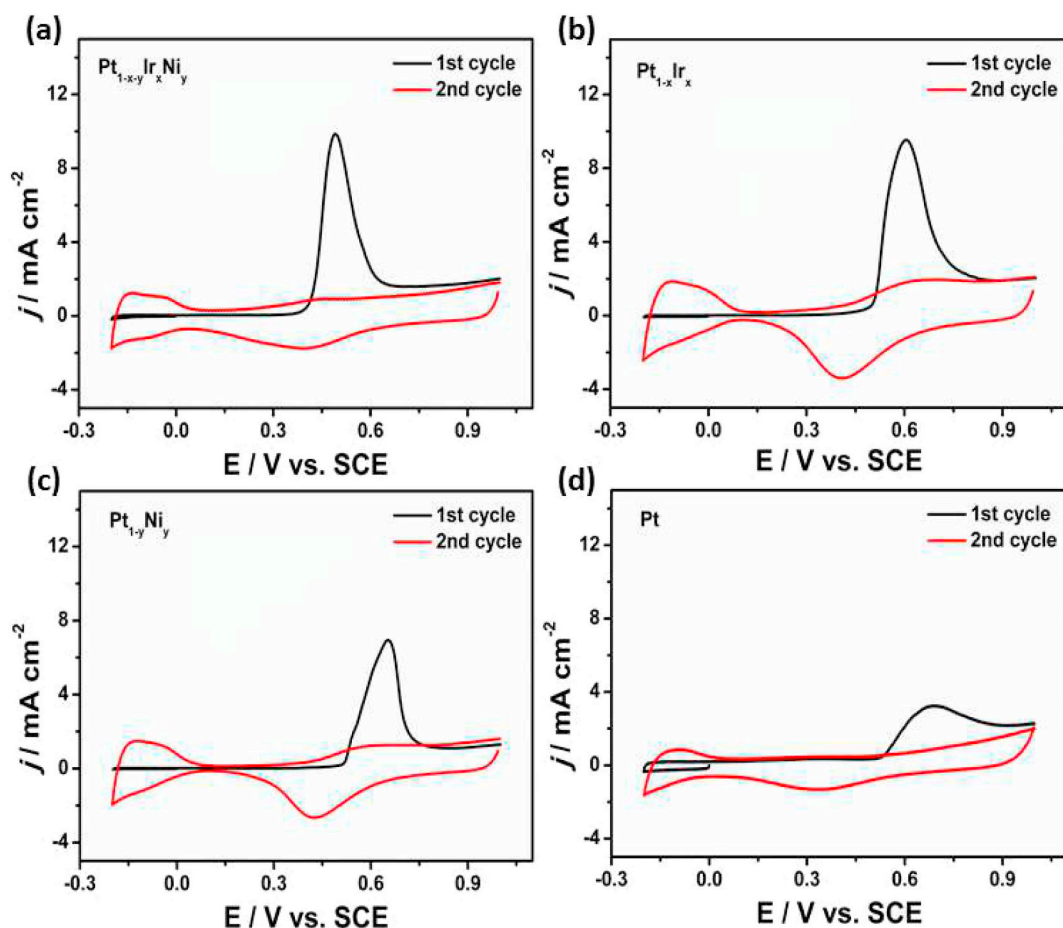
Fig. 5. CO stripping Voltammograms of (a) $Pt_{1-x-y}Ir_xNi_y$, (b) $Pt_{1-x}Ir_x$, (c) $Pt_{1-y}Ni_y$, and (d) Pt recorded in 0.1 M $HClO_4$ solution.

(SCE) in case of $Pt_{1-x}Ir_x$, $Pt_{1-y}Ni_y$, and Pt, respectively. The negative shift in the onset potential of the ternary catalyst compared to other counterparts confirms the enhancement in ethanol oxidation reaction, EOR kinetics over other Pt-based catalysts. The catalytic activity of different electrocatalysts was estimated on the basis of mass activity measured at the peak current density of the forward scan. The $Pt_{1-x-y}Ir_xNi_y$ depicted a mass activity of $3.8\,A\,mg_{Pt}^{-1}$, whereas its specific activity is $5.2\,mA\,cm^{-2}$.

The ratio of forward peak current density, j_f to backward peak current density, j_b is a measure for the poisoning tolerance of the electrocatalyst [2]. The $Pt_{1-x-y}Ir_xNi_y$ exhibited a great value for j_f/j_b of 4.5, while $Pt_{1-x}Ir_x$, $Pt_{1-y}Ni_y$, and Pt showed values of 2.3, 1.1, and 1.2, respectively. The high value of j_f/j_b in case of ternary electrocatalyst confirms efficient oxidation for ethanol in the forward scan with little adsorption of the reaction intermediates [28]. All electrochemical parameters of mono, binary, and ternary catalysts are summarized in Table 2. The CO poisoning tolerance was further investigated by CO stripping voltammetry (Fig. 5). For all electrocatalysts CO was completely oxidized in the first scan and no oxidation peak was observed in the second sweep. The onset potential and the peak potential of $Pt_{1-x-y}Ir_xNi_y$ was negatively shifted compared to mono and binary counterparts revealing its prominent anti CO-poisoning performance. The obtained results confirm the outstanding performance of our ternary electrocatalyst towards ethanol electro-oxidation besides its prominent poisoning tolerance relative to many reported binary and ternary Pt-based alloys (see Supplementary Table S1).

The stability of an electrocatalyst is an indispensable parameter for its commercialization in fuel cell applications. Fig. 4c represents the initial mass activities of different electrocatalysts compared to their values measured after 1000 durability cycles. It is clearly evident that

the $Pt_{1-x-y}Ir_xNi_y$ depicts the highest stability with 2.3% decay in the initial activity compared to $Pt_{1-x}Ir_x$, $Pt_{1-y}Ni_y$, and Pt, which displayed decay percentages of about 10, 31, and 43%, respectively (Fig. 4c). This is harmonious with the stability in the ECSA of all catalysts after 1000 durability cycles (see Supplementary Fig. S3), where $Pt_{1-x-y}Ir_xNi_y$ showed 9% decay in the active surface compared to 18, 31, and 39% decay in case of $Pt_{1-x}Ir_x$, $Pt_{1-y}Ni_y$, and Pt, respectively. Fig. 4d depicts the chronoamperometric responses of different electrocatalysts measured at a potential of $-0.2\,V$ vs. SCE. The observed decay in the current density with time for all electrocatalysts is attributed to the CO-like intermediates formed during the ethanol oxidation and lead to blocking or deactivation of the active sites with time. After 60 min durability test, $Pt_{1-x-y}Ir_xNi_y$ ternary alloy exhibited the lowest rate of decay in the current density, which confirms its outstanding stability compared to other counterparts.

Because of the more positive redox potential of Pt and Ir relative to Ni, the reduction step is initiated with the preferential formation of Pt and Ir nuclei in the early stages of the reaction enhanced by their faster reduction kinetics [29,30]. F127 molecules are self-assembled on the surface of the formed nuclei driving the formation of a porous structure. Absence of F127 can lead to agglomeration of the formed nuclei and formation of non-porous randomly-shaped aggregates in the micrometer scale [31,32]. The formed nuclei induce the reduction of Ni^{2+} vis autocatalytic effect to form porous ternary dendritic nanocrystals. The enhanced Electrocatalytic performance of $Pt_{1-x-y}Ir_xNi_y$ towards ethanol oxidation in alkaline media can be attributed to the synergy between different alloying elements: Ni eases the formation of oxygenated species such as $(OH)_{ads}$ at low overpotentials which minimize the poisoning impact of CO species, and Ir weakens the binding of CO_{ads} and CO-like intermediates [33].

4. Conclusion

We demonstrated a simple one-step room temperature synthesis of ternary $Pt_{1-x-y}Ir_xNi_y$ nanocrystals electrocatalyst. It is based on co-reduction of the metal precursors using ascorbic acid as a mild reducing agent and use of pluronic F127 as a structure-directing agent. This synthesis approach drove the formation of a porous nanodendritic morphology with an average particle size of 20 ± 1 nm. The ternary nanocrystals show superior electrocatalytic activity and durability towards oxidation of ethanol in alkaline media compared to binary and mono counterparts. The outstanding performance of this Pt-based ternary electrocatalyst was ascribed to its unique composition and morphology. The porous structure with high fraction of surface atoms with lower coordination at the nanodendrites branches and the synergistic effect of different alloying elements promote considerably improved catalytic activity, poisoning tolerance (j_f/j_b = 4.5), and durability for this ternary electrocatalyst compared to binary and mono counterparts.

Acknowledgements

Appendix A. Supplementary data

Supplementary data to this article can be found online at https://doi.org/10.1016/j.elecom.2019.03.001.

References

[1] L. Cao, G. Sun, H. Li, Q. Xin, Electrochem. Commun. 9 (2007) 2541–2546.
[2] H. Gao, S. Liao, Z. Liang, H. Liang, F. Luo, J. Power Sources 196 (2011) 6138–6143.
[3] Z. Zhang, L. Xin, K. Sun, W. Li, Int. J. Hydrog. Energy 36 (2011) 12686–12697.
[4] W. Huang, H. Wang, J. Zhou, J. Wang, P.N. Duchesne, D. Muir, P. Zhang, N. Han, F. Zhao, M. Zeng, Nat. Commun. 6 (2015) 10035.
[5] H. Liu, C. Song, L. Zhang, J. Zhang, H. Wang, D.P. Wilkinson, J. Power Sources 155 (2006) 95–110.
[6] Y. Zheng, J. Qiao, J. Yuan, J. Shen, A.-J. Wang, S. Huang, Int. J. Hydrog. Energy 43 (2018) 4902–4911.
[7] A. Velázquez-Penzuela, E. Brillas, C. Arias, F. Centellas, J.A. Garrido, R.M. Rodríguez, P.-L. Cabot, J. Power Sources 225 (2013) 163–171.
[8] P. Song, L.-P. Mei, A.-J. Wang, K.-M. Fang, J.-J. Feng, Int. J. Hydrog. Energy 41 (2016) 1645–1653.
[9] T. Liu, K. Wang, Q. Yuan, Z. Shen, Y. Wang, Q. Zhang, X. Wang, Nanoscale 9 (2017) 2963–2968.
[10] A. Ruban, B. Hammer, P. Stoltze, H.L. Skriver, J.K. Nørskov, J. Mol. Catal. A Chem. 115 (1997) 421–429.
[11] L.-X. Dai, X.-Y. Wang, S.-S. Yang, T. Zhang, P.-J. Ren, J.-Y. Ye, B. Nan, X.-D. Wen, Z.-Y. Zhou, R. Si, J. Mater. Chem. A 6 (2018) 11270–11280.
[12] D. Chai, W. Wang, F. Wang, W. Jing, P. Wang, Z. Lei, Int. J. Hydrog. Energy 42 (2017) 9775–9783.
[13] R. Loukrakpam, S. Shan, V. Petkov, L. Yang, J. Luo, C.-J. Zhong, J. Phys. Chem. C 117 (2013) 20715–20721.
[14] E.N. El Sawy, V.I. Birss, ACS Appl. Mater. Interfaces 10 (2018) 3459–3469.
[15] Q. Jiang, L. Jiang, H. Hou, J. Qi, S. Wang, G. Sun, J. Phys. Chem. C 114 (2010) 19714–19722.
[16] J. Ribeiro, D. Dos Anjos, K.B. Kokoh, C. Coutanceau, J.-M. Léger, P. Olivi, A. De Andrade, G. Tremiliosi-Filho, Electrochim. Acta 52 (2007) 6997–7006.
[17] H. Lv, A. Lopes, D. Xu, B. Liu, ACS Cent. Sci. 4 (2018) 1412–1419.
[18] H. Lv, L. Sun, L. Zou, D. Xu, H. Yao, B. Liu, Chem. Sci. (2019), https://doi.org/10.1039/c8sc04696d.
[19] S. Liao, K.-A. Holmes, H. Tsaprailis, V.I. Birss, J. Am. Chem. Soc. 128 (2006) 3504–3505.
[20] V. Malgras, H. Ataee-Esfahani, H. Wang, B. Jiang, C. Li, K.C.W. Wu, J.H. Kim, Y. Yamauchi, Adv. Mater. 28 (2016) 993–1010.
[21] H. Ataee-Esfahani, L. Wang, Y. Nemoto, Y. Yamauchi, Chem. Mater. 22 (2010) 6310–6318.
[22] J.S. Jeong, M.L. Odlyzko, P. Xu, B. Jalan, K.A. Mkhoyan, Phys. Rev. B 93 (2016) 165140.
[23] J.S. Jeong, K.A. Mkhoyan, Microsc. Microanal. 22 (2016) 536–543.
[24] M. Li, D.A. Cullen, K. Sasaki, N.S. Marinkovic, K. More, R.R. Adzic, J. Am. Chem. Soc. 135 (2012) 132–141.
[25] X.-Y. Huang, A.-J. Wang, L. Zhang, K.-M. Fang, L.-J. Wu, J.-J. Feng, J. Colloid Interface Sci. 531 (2018) 578–584.
[26] J.L. Tan, A.M. De Jesus, S.L. Chua, J. Sanetuntikul, S. Shanmugam, B.J.V. Tongol, H. Kim, Appl. Catal. A Gen. 531 (2017) 29–35.
[27] Q. Wang, Y. Liao, H. Zhang, J. Li, W. Zhao, S. Chen, J. Power Sources 292 (2015) 72–77.
[28] W. Liu, A.K. Herrmann, D. Geiger, L. Borchardt, F. Simon, S. Kaskel, N. Gaponik, A. Eychmüller, Angew. Chem. Int. Ed. 51 (2012) 5743–5747.
[29] H. Kwon, M.K. Kabiraz, J. Park, A. Oh, H. Baik, S.-I. Choi, K. Lee, Nano Lett. 18 (2018) 2930–2936.
[30] K. Eid, Y.H. Ahmad, H. Yu, Y. Li, X. Li, S.Y. AlQaradawi, H. Wang, L. Wang, Nanoscale 9 (2017) 18881–18889.
[31] B. Jiang, C. Li, V. Malgras, M. Imura, S. Tominaka, Y. Yamauchi, Chem. Sci. 7 (2016) 1575–1581.
[32] K. Deng, Y. Xu, C. Li, Z. Wang, H. Xue, X. Li, L. Wang, H. Wang, Langmuir 35 (2018) 413–419.
[33] J.-M. Jin, T. Sheng, X. Lin, R. Kavanagh, P. Hamer, P. Hu, C. Hardacre, A. Martinez-Bonastre, J. Sharman, D. Thompsett, Phys. Chem. Chem. Phys. 16 (2014) 9432–9440.